Landscape and Urban Planning 204 (2020) 103927

Contents lists available at ScienceDirect

Landscape and Urban Planning

journal homepage: www.elsevier.com/locate/landurbplan

Assessing the thermal contributions of urban land cover types

Jiacheng Zhao[a], Xiang Zhao[a,*], Shunlin Liang[b], Tao Zhou[c,d], Xiaozheng Du[a], Peipei Xu[e], Donghai Wu[f,*]

[a] State Key Laboratory of Remote Sensing Science, Jointly Sponsored by Beijing Normal University and Institute of Remote Sensing and Digital Earth of Chinese Academy of Sciences, Faculty of Geographical Science, Beijing Normal University, Beijing 100875, China
[b] Department of Geographical Sciences, University of Maryland, College Park, MD 20742, USA
[c] Key Laboratory of Environmental Change and Natural Disaster of Ministry of Education, Academy of Disaster Reduction and Emergency Management, Faculty of Geographical Science, Beijing Normal University, Beijing 100875, China
[d] State Key Laboratory of Earth Surface Processes and Resource Ecology, Beijing Normal University, Beijing 100875, China
[e] College of Geography and Tourism, Anhui Normal University, Wuhu 241002, China
[f] Department of Ecology and Evolutionary Biology, Cornell University, Ithaca, NY 14853, USA

ARTICLE INFO

Keywords:
Land surface temperature
Elastic net regression
Urban land cover
Thermal contribution assessment
Beijing metropolitan region

ABSTRACT

Understanding the thermal contribution of urban land cover is crucial for alleviating urban heat islands (UHIs). Extensive work has assessed this contribution by estimating the responses of heat-related variables, such as land surface temperature (LST), to landscape patterns in terms of composition and configuration. However, ignoring the endogenous collinearity in landscape composition may lead to biased estimations. In this study, an elastic net regularized regression was used to disentangle the thermal contributions (i.e, the local cooling/warming effects) of six urban land cover types (i.e., water body, urban tree, grassland, bare land, impervious surface, and building) in the Beijing metropolitan region of China. In addition, the benefits of cooling/warming gains from the spatial aggregation of vegetation/buildings were quantified. The results indicate that for a 10% increase in coverage within an area of 1440 × 1440 m^2, buildings appear to have a strong warming effect and raise local LST by ~1.26 ℃, which is much higher than the warming caused by impervious surfaces (~0.23 ℃). In contrast, water bodies, grasslands, and urban trees have different cooling effects that reduce local LST by ~0.72 ℃, ~0.60 ℃ and ~0.57 ℃, respectively. Landscape configuration interactively affects local LST based on the composition. The aggregation cooling (~-1.2 ℃ at maximum) of vegetation only takes effect when the local vegetation coverage is less than 40%. The aggregation warming (~1.3 ℃ at maximum) of buildings occurs when the local building coverage is more than 15%. These findings provide new insights into the thermal contribution assessment of urban land cover that helps create urban heat island (UHI) mitigation strategies and plan future landscapes.

1. Introduction

Urbanization of natural lands has caused various types of environmental deterioration worldwide (Jaeger et al., 2010). An increase in built-up areas of 1.2 million km^2 is forecasted by 2030, which nearly triples the global urban cover as of 2000 (Seto et al., 2012). Land use and land cover (LULC) changes notably disturb the land-atmosphere energy budget and consequently bring about urban heat islands (UHIs) (Grimm et al., 2008), which represent the phenomenon of a much warmer temperature in an urban area than its surrounding rural areas (Streutker, 2003). Warm temperatures promote the turbulent dispersion of air pollutants and accelerate energy consumption (Li, Meier, & et al., 2018; Palme et al., 2017). According to Santamouris et al. (2015), approximately 0.5–8.5% of electricity demand is required to compensate for each degree of ambient temperature increase. In addition, the UHI effect poses threats to public health by increasing morbidity and mortality (Taylor et al., 2015), especially during heat waves (Anderson and Bell, 2010; Ostro et al., 2009). Nearly a third of the world's population is regularly exposed to deadly heat, and the number is continuously growing (Mora et al., 2017).

Extensive work related to the UHI effect has been carried out at multiple scales ranging from microclimate investigations (Gros et al., 2016; Jenerette et al., 2016; Razzaghmanesh et al., 2016) to UHI spatial-temporal variations (Deilami et al., 2018; Haashemi et al., 2016; Miles and Esau, 2017). At microscale, by simulating the interaction of a building with its surrounding environment, computational fluid

* Corresponding authors at: No. 19, XinJieKouWai St., HaiDian District, Beijing 100875, PR China (X. Zhao). Corson Hall, Ithaca, NY 14850, USA (D. Wu).
E-mail addresses: zhaoxiang@bnu.edu.cn (X. Zhao), dw623@cornell.edu (D. Wu).

https://doi.org/10.1016/j.landurbplan.2020.103927
Received 6 September 2019; Received in revised form 3 August 2020; Accepted 8 August 2020

dynamics-based models (e.g., ENVI-met) along with *in situ* measurements are generally utilized to inspect the thermal comfort regime for block/street canyon layers with different surface materials and geometries (O'Malley et al., 2015; Qaid et al., 2016; Rajagopalan et al., 2014). At the mesoscale, which also refers to the city scale, researchers have explored the relationship between heat-related variables, e.g., land surface temperature (LST), air temperature and landscape patterns, in terms of composition and configuration (Li et al., 2016; Peng et al., 2016). Composition represents the variety and abundance of a landscape, while configuration focuses on the geometric characteristics and spatial arrangements of patches within a landscape (McGarigal and Marks, 1995). At the global scale, satellite images are widely used for long-term monitoring of the occurrence and development of UHI intensity (Chakraborty and Lee, 2019; Peng et al., 2012). Cities with different hydroclimatic conditions have shown distinct diurnal and seasonal behaviors of UHI (Lai et al., 2018; Manoli et al., 2019; Shastri et al., 2017).

Strategies for UHI mitigation based on landscape optimization have become a focus of urban ecology (Iping et al., 2019; Myint et al., 2015). Almost all associated studies agree that increasing blue/greenspaces while decentralizing built-up areas have potential benefits for thermal stress alleviation (Duncan et al., 2019; Hamoodi et al., 2019; Li, Zhou, & et al., 2018; Li et al., 2011; Shirani-Bidabadi et al., 2019; Ullah et al., 2019). However, the efficient implementation of UHI strategies continues to be challenging (Parsaee et al., 2019). One barrier to these strategies could be that the impact of landscape pattern on UHIs is still debatable. Although some studies emphasize that composition plays a more critical role than configuration (Chen and Yu, 2017; Maimaitiyiming et al., 2014; Zhou et al., 2011), others do not (Du et al., 2016; Zhou et al., 2017). Therefore, the effects of both composition and configuration, as well as their interactions, should be further explored.

Diverse empirical analyses are employed to quantify the response of LST to landscape composition/configuration. The ordinary least squares (OLS) regression (Connors et al., 2013; Li et al., 2012) is commonly used for its simplicity. Geographically weighted regression (GWR) (Buyantuyev and Wu, 2010) performs well within spatially varying relationships (Fotheringham et al., 2002). Mixed-effect models (Du et al., 2016) are also introduced to estimate the hierarchical effects of landscape patterns on LST. Spatial regressions (Chun and Guldmann, 2014; Song et al., 2014) generally account for the autocorrelation of dependent variables by the spatial lag model (SLM) or that of random errors by the spatial error model (SEM). Despite the remarkable contributions of these works, two issues remain to be resolved. First, previous studies (Estoque et al., 2017; Hao et al., 2016; Li et al., 2011; Ma et al., 2016; Zhang and Sun, 2019) commonly investigated the relationship between the LST and the proportion of vegetation or impervious area by ignoring other types (e.g., water body or bare land), which also have thermal contributions. Such ignoration, especially in complex landscapes, may lead to a biased thermal contribution estimation because a local thermal environment is formed by heat exchange among multiple surface types in the physics of land processes. More importantly, the thermal contributions of other land cover types are unable to be assessed. The second issue develops based on the first. Assuming that we model the LST variation using all coexisted land cover types, a problem of the perfect collinearity arises (Chen et al., 2010). Since a particular area with high vegetation coverage inevitably has a low coverage of other types, such structural collinearity leads to a synergistic effect of explanatory variables on the response (Graham, 2003). This effect increases the sensitivity of regression coefficients, which is manifested as a small change in variables could cause wide variations in coefficients, resulting in wrong signs and irrational magnitudes for some regressors (Kmita et al., 2002; Parkin et al., 2002; Tu et al., 2005; Yoo et al., 2014). Consequently, the thermal contribution of each land cover type can hardly be disentangled without considering this multicollinearity.

The objectives of this research are to assess the thermal contributions of multiple urban land cover types from the perspectives of composition and configuration. Specifically, we aim to (1) model the LST-composition relationship with the elastic net regression, which addresses the multicollinearity to disentangle the thermal contributions of multiple land cover types; (2) detach the effect of configuration from that of composition based on the established model in (1); and (3) investigate how composition and configuration interactively affect LST. The thermal contribution of land cover is reflected in the combined effect of composition and its spatial features.

2. Materials and methods

2.1. Study area

Beijing is the capital of China, covering an area of 16,808 km^2. It is located on the North China Plain at latitudes of 39°28′N to 41°05′N and longitudes of 115°25′E to 117°30′E. Although ringed by mountains, the city lies on low and flat land with elevations generally between 40 and 60 m above sea level. Beijing experiences a monsoon-influenced humid continental climate, making the summer rainy and hot and the winter dry and cold. Rapid urbanization and economic development in recent decades have led to drastic LULC changes. From 1987 to 2013, the built-up areas had increased by more than three times (Han et al., 2015), which contributes to an urbanization rate of 86.4% in 2014 (Zhang et al., 2015). At the end of 2017, the permanent residential population of Beijing had reached 21.7 million (Beijing Municipal Bureau Statistics, 2018).

With the implementation of the Beijing Outline of the Eleventh Five-Year Program for National Economic and Social Development (2006–2010) (2006) and the Beijing General Planning (2004–2020) (2005), the previous 16 administrative districts have now been merged into four functional zones (Fig. 1b): the Core Function Zone (I), the Urban Function Extended Zone (II), the New Urban Development Zone (III) and the Ecological Conservation Zone (IV). The Core Function Zone includes the inner city that mainly consists of historical sites, old residential buildings, and corporate headquarters. This zone is also the most urbanized area in Beijing. The Urban Function Extended Zone holds most technology parks, large forest parks, universities, and central business districts, thus becoming a center for commercial and international communication. These two zones provide us better footage for urban thermal environment investigation with various surface materials and complicated landscape patterns. Thus, we conducted the study in the Beijing metropolitan region (shaded area in Fig. 1b), covering the Core Function Zone and most of the Urban Function Extended Zone.

2.2. Land cover mapping

We used four cloud-free Gaofen-2 (GF-2) images acquired on June 9, 2017, for land cover mapping. They were first orthorectified and then mosaicked for standard processing including radiation calibration, atmospheric correction, and geometric correction. A panchromatic band was used to sharpen the multispectral bands with the nearest-neighbor diffusion pan-sharpening algorithm (Sun et al., 2014), which gave us a 1-m fused image.

Per-pixel classification is commonly used for land cover mapping, for example, the maximum likelihood of parametric classifiers and support vector machines, decision trees as well as random forest of nonparametric classifiers. The latter outperforms the former for its capacity to noise processing, compatibility in multisource datasets without overfitting (Breiman, 2001), and higher classification accuracy (Foody, 2002; Rodriguez-Galiano et al., 2012). Bagging and boosting such as the extreme gradient boosting (Abdullah et al., 2019) are also used as a feature selection tool to enhance nonparametric classifications (Lu and Weng, 2007).

However, when dealing with fine-resolution images, pixel-based

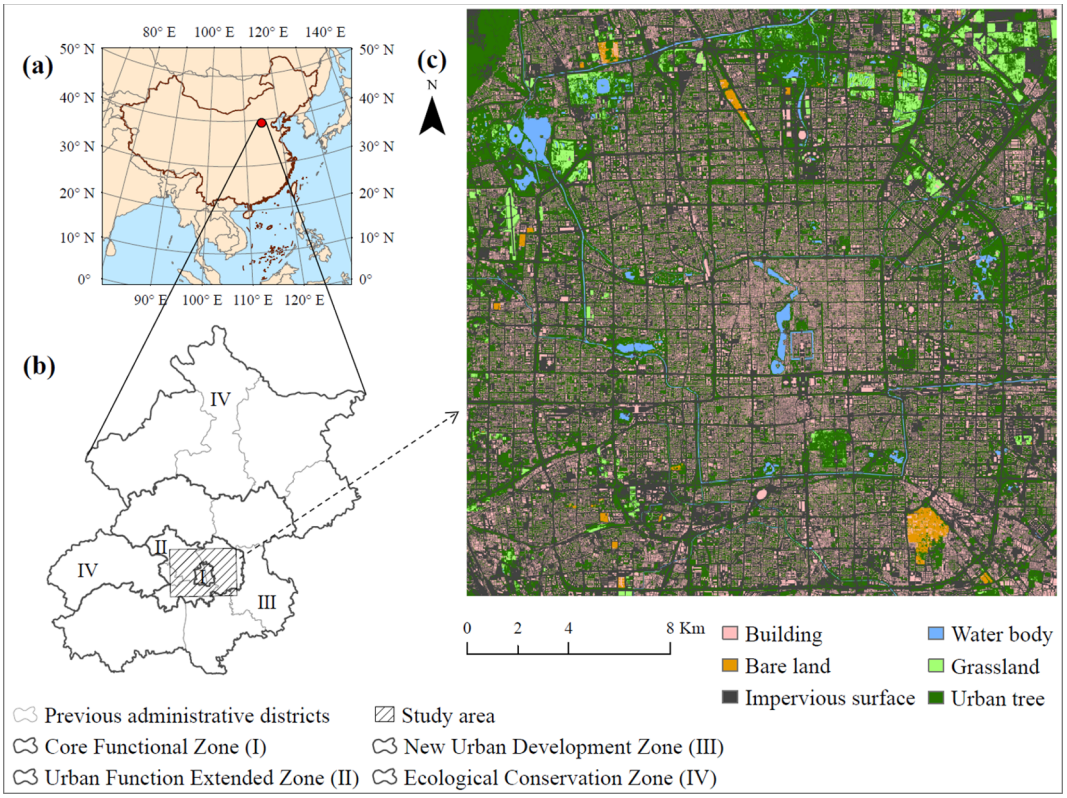

Fig. 1. Location of Beijing in China and land cover map of the study area. (a) Location of Beijing, China. (b) Previous and new administrative districts in Beijing. (c) Land cover map of the study area derived from GF-2 images in 2017 with a spatial resolution of 1 m.

Table 1
Descriptions of the urban land cover types in the study.

Land cover types	Descriptions
Water body	Canals, rivers, lakes, ponds, reservoirs and any other open water
Urban tree	General urban vegetation with a certain height and canopy geometry, mainly including arbors, shrubs, bamboos, etc.
Grassland	Grass planted in parks, lawns for ornamental use and recreation, open lands with weeds and other green patches
Bare land	Lands that are not covered either by vegetation or artificial materials, generally unmanaged construction sites, and exposed soils
Impervious surface	Streets, highways, railways, pavements, parking lots that are made of asphalt, concrete, and ceramic tile
Building	Built-up areas including residences, commercial districts, and public facilities

classification methods might perform inefficiently due to the complexity of spectral responses from small objects (Myint et al., 2011) and the lack of consideration of spatial information (Walter, 2004). In contrast, object-based image analysis methods spatially segment adjacent and spectrally similar pixels into small objects, hence achieving higher accuracy. We initially used eCognition 9.0 software to classify the fused image into several classes, including urban tree, water, building, shadow, grassland, shrub, bare land, pavement and artificial surface. Then, they were merged into six urban land cover types based on their physical properties and effects on LST (Du et al., 2016) (Fig. 1c): water body, urban tree, grassland, bare land, impervious surface and building. To verify the classification accuracy, we randomly generated two hundred validation points within the land cover map. Each point was tagged with true land cover labels based on high-resolution Google Earth historical images. A land cover on-the-spot investigation was also carried out for the points that could not be visually interpreted. The overall classification accuracy is 85.5% according to the confusion matrix for the land cover map (Table S1 in supplementary data). Table 1 represents the detailed descriptions of the six types.

2.3. LST retrieval

Various algorithms retrieving LST from satellite data have been developed, for example, single-channel algorithms, multichannel/angle algorithms, temperature emissivity separation methods, and artificial neural network-based methods (Li, Tang, & et al., 2013). Since the Thermal Infrared Sensor (TIRS) of Landsat 8 has two thermal bands (i.e., band 10 and band 11), multichannel approaches, e.g., split-window algorithms, should be adopted to achieve more accurate results compared to single-channel algorithms (Jiménez-Muñoz et al., 2014). However, stray light artifacts in TIRS data has been determined, and the magnitude of induced radiometric calibration errors in band 11 was found to be roughly twice as they are in band 10 (Montanaro et al., 2014). Hence, the LST in this study was retrieved from the Landsat 8 band 10.

A Landsat 8 image (scene ID LC81230322017191LGN00) with cloud cover less than 2% was used to retrieve LST, which was acquired on July 10, 2017, from the U.S. Geological Survey (USGS). The raw digital number of the Landsat 8 band 10 was first converted to at-sensor brightness temperature, and a generalized single-channel (SC) algorithm (Jiménez-Muñoz et al., 2008) was then employed to estimate LST (T_s) using the following equation

$$T_s = \gamma\left[\frac{1}{\varepsilon}(\psi_1 L_{sen} + \psi_2) + \psi_3\right] + \delta \quad (1)$$

where L_{sen} is the at-sensor radiance, ε is the surface emissivity, γ and δ

are given by

$$\gamma = \left[\frac{c_2 L_{sen}}{T_{sen}^2}\left(\frac{\lambda^4 L_{sen}}{c_1} + \frac{1}{\lambda}\right)\right]^{-1} \quad (2)$$

$$\delta = -\gamma L_{sen} + T_{sen} \quad (3)$$

with $c_1 = 1.19104{\cdot}10^8$ W · μm^4 · m^{-2} · sr^{-1} and $c_2 = 14387.7$ μm · K being the Planck's radiation constants. T_{sen} is the at-sensor brightness temperature, and λ refers to the effective wavelength of the Landsat 8 band 10 (10.904 μm). ψ_1, ψ_2 and ψ_3 are the atmospheric functions estimated from the atmospheric water vapor content (w, in g/cm^2) by

$$\begin{bmatrix}\psi_1\\ \psi_2\\ \psi_3\end{bmatrix} = \begin{bmatrix}c_{11} & c_{12} & c_{13}\\ c_{21} & c_{22} & c_{23}\\ c_{31} & c_{32} & c_{33}\end{bmatrix}\begin{bmatrix}w^2\\ w\\ 1\end{bmatrix} \quad (4)$$

with the matrix coefficients c_{11}, c_{12}, …, c_{33} derived from the Global Atmospheric Profiles from Reanalysis Information (GAPRI) database (Jiménez-Muñoz et al., 2014; Mattar et al., 2015).

The atmospheric water vapor content was acquired from the level-2 Water Vapor (pre- and post-field calibrated, cloud-screened, and quality-assured) by NASA's Aerosol Robotic Network (Giles et al., 2019), which is available online (http://aeronet.gsfc.nasa.gov). The water vapor value at the Landsat acquisition time was approximated by using the closest data of the site "Beijing-CAMS" (39.93°N, 116.32°E) on July 10, 2017.

Surface emissivity is a critical parameter for LST retrieval. Based on the emissivity correction procedure given by Malakar et al. (2018), the emissivity was first spectrally adjusted (ε_{adj}) from ASTER GED v3 (available at https://lpdaac.usgs.gov/products/ag100v003/) by

$$\varepsilon_{adj} = c_{13}\varepsilon_{13} + c_{14}\varepsilon_{14} + c \quad (5)$$

where c_{13}, c_{14}, and c are the regression coefficients, and ε_{13} and ε_{14} are the ASTER GED v3 emissivity values for band 13 and 14, respectively. Then, it was dynamically adjusted accounting for vegetation phenology by

$$\varepsilon = f_{v,Landsat}\,\varepsilon_{veg} + (1 - f_{v,Landsat})\varepsilon_{bare} \quad (6)$$

where

$$\varepsilon_{bare} = \frac{\varepsilon_{adj} - \varepsilon_{veg} f_{v,ASTER}}{1 - f_{v,ASTER}} \quad (7)$$

where ε_{veg} is the vegetation emissivity, which is set to 0.98, ε_{bare} is the estimated ASTER bare soil emissivity, and $f_{v,Landsat/ASTER}$ is the fractional vegetation cover (FVC) corresponding to the normalized difference vegetation index (NDVI) of Landsat or ASTER.

2.4. Thermal contribution of land cover composition

To evaluate the thermal contributions of various land cover types, we established a linear relationship between the land cover fraction and local LST over a moving window as follows

$$\begin{bmatrix}y_1\\ y_2\\ \vdots\\ y_n\end{bmatrix} = \begin{bmatrix}1 & x_{11} & \dots & x_{1k}\\ 1 & x_{21} & \dots & x_{2k}\\ \vdots & \vdots & \ddots & \vdots\\ 1 & x_{n1} & \dots & x_{nk}\end{bmatrix}\begin{bmatrix}\beta_0\\ \beta_1\\ \vdots\\ \beta_k\end{bmatrix} + \begin{bmatrix}\varepsilon_1\\ \varepsilon_2\\ \vdots\\ \varepsilon_n\end{bmatrix} \quad (8)$$

where x_{ij} is the jth land cover fraction in the ith window for n windows and k land cover types, y is the mean local LST averaged by all LST pixels over the window (for convenience, denoted as LST* in the following text), β is the regression coefficients, and ε is the error term. A positive sign of β_j indicates that LST* increases as the jth land cover fraction increases, which means that the jth land cover has a positive thermal contribution (local warming effect). A negative sign of β_j denotes that LST* decreases as the jth land cover fraction increases, which means that the jth land cover has a negative thermal contribution (local cooling effect).

If we directly solve Eq. (8) by using the OLS method, the resulting $\hat{\beta}$ are estimated by minimizing the sum of the squared residuals

$$\sum_{i=1}^{n}(y_i - \beta_0 - \sum_{j=1}^{k} x_{ij}\beta_j)^2 \quad (9)$$

However, since all land covers within the window were considered, a perfect collinearity (Chen et al., 2010) exists in the land cover fractions, i.e., $x_{i1} + x_{i2} + \ldots + x_{ik} = 1$. Elastic net regression (Zou and Hastie, 2005) was accordingly employed to address such collinearity by adding the lasso penalty $\lambda\sum_{j=1}^{k}|\beta_j|$ and ridge penalty $\lambda\sum_{j=1}^{k}\beta_j^2$ to the loss function (Eq. (10)). Lasso can be regarded as a selection operator that shrinks absolutely by forcing the coefficients with minor contributions to exactly zero, while the ridge shrinks the coefficients with minor contributions to approach zero but retains them all (Lenters et al., 2015). Elastic net is a novel shrinkage that bridges the ridge and lasso regression, and it outperforms lasso on highly correlated data (Zou and Hastie, 2005). The elastic net regression gives $\hat{\beta}$ by minimizing the follows

$$\sum_{i=1}^{n}\left(y_i - \beta_0 - \sum_{j=1}^{k} x_{ij}\beta_j\right)^2 + \lambda\left(\alpha\sum_{j=1}^{k}|\beta_j| + (1-\alpha)\sum_{j=1}^{k}\beta_j^2\right) \quad (10)$$

where λ defines the extent to which the coefficients shrink, and α is the mixing parameter ranging from 0 to 1. These two tunable parameters were optimized by cross-validation (Candia and Tsang, 2019; Waldmann et al., 2013). Despite the employment of the elastic net regression, the simple regression and multiple regression based on the OLS method were also conducted for comparison.

The size of the moving window needs to be carefully considered since most adjacent geographic variables (e.g., LSTs in our case) are spatially autocorrelated, which violates the basic regression assumption that observations are independent of one another. To address the spatial autocorrelation of LSTs, we followed the framework given by Song et al. (2014) to find the most suitable size from 240 m × 240 m to 2400 m × 2400 m. A size of 1440 m × 1440 m was finally chosen as our optimized window size over which the impact of spatial autocorrelation on the model coefficients was minimized (see Table S2 in supplementary data).

2.5. Thermal contribution of land cover configuration

When characterizing the effect of landscape configuration, urban trees and grassland were equally treated as "vegetation" because they are generally planted together, and a separate calculation would be redundant and ambiguous. Moreover, we only considered the spatial features of vegetation and buildings due to their relatively high coverage. Due to a stronger correlation with LST compared to other spatial metrics such as patch size and shape complexity (Estoque et al., 2017), aggregation index (AI, Table 2) and mean of the Euclidean nearest-neighbor distance (ENN, Table 2) were chosen as the surrogate for landscape configuration. AI is an adjacency matrix and a single-count-based calculation. It is suitable for describing vegetation aggregation since the canopies of aggregated trees are very close to each other, making them readily grouped into one single compact patch. In such a case, AI approaches its maximum (Fig. S1a, b). However, only considering adjacency while ignoring the distance between patches resulted in a "pseudo" building aggregation indicated by a higher AI (Fig. S1c, d). ENN, which is distance-based, was therefore employed to better reflect building aggregation (Fig. S1c, d).

To minimize the effect of landscape composition, we investigated the effect of spatial aggregation for different FVC levels from 10% to 50% (Table 3). All the windows with more than 50% vegetation coverage were grouped to one level due to a smaller sample size. At each FVC level, the effect of composition was assumed to be the same and

Table 2
Spatial metrics employed in this study and how they characterize spatial aggregation.

Spatial metrics	Descriptions & Behaviors
Aggregation index (AI)	Equals the number of like adjacencies divided by the theoretical maximum possible number of like adjacencies for that class and multiplied by 100 Ranges from 0 to 100. Equals 0 for maximally isolated, i.e., when no like adjacencies were found. Equals 100 for maximally aggregated, i.e., all the patches of the same class are adjacent to each other and clumped into one single compact patch
Mean of Euclidean nearest-neighbor distance (ENN)	Measures the edge-to-edge distance to the nearest neighboring patch of the same class Approaches 0 as the distance to the nearest neighbor decreases, i.e., patches of the same class are more aggregated. Increases without limit, as the distance between neighboring patches of the same class increases, i.e., patches are more isolated

expressed by the established elastic net model

$$y'_m = \beta_0 + \sum_{j=1}^{k} \bar{x}_{mj}\beta_j \tag{11}$$

where $\bar{x}_{mj}$ is the mean fraction of the jth land cover type in all windows on the mth FVC level, and y'_m is the theoretical average LST* on the mth FVC level. For each FVC level, the difference between the LST* and the theoretical average LST* could be defined as the aggregation effect (AE)

$$AE = y_{mi} - y'_m = y_{mi} - \beta_0 - \sum_{j=1}^{k} \bar{x}_{mj}\beta_j \tag{12}$$

where y_{mi} is the LST* of the ith window on the mth FVC level. A positive value of AE represents aggregation warming, while a negative value of AE represents aggregation cooling.

To minimize the uncertainty of the thermal contribution of configuration induced by other factors such as the difference in tree species and anthropogenic heats, we inspected the relationships between LST*/AE and spatial metrics at each FVC level by the binned average analysis (Huang et al., 2015). The values of LST*/AE were binned according to their corresponding AI (0.1) and ENN (0.3) bins.

3. Results

3.1. Characteristics of LST by land cover types

LST is directly related to the land cover types. Fig. 2a depicts the pattern of LSTs for the Beijing metropolitan region in the summer of 2017. UHI areas of different intensities were distributed from downtown to suburbs and highly correlated with the fraction of buildings and urban trees (Fig. 2b). The UHI effect in southern Beijing was more intensive than that in northern Beijing. Severe UHI areas generally occurred in densely populated areas with high impervious covers (including impervious surfaces and buildings), such as the inner city (Core Function Zone) and southeast/southwest Urban Function Extended Zone (Fig. 1). Some extreme cases with LSTs around 50 ℃ were sporadically scattered, such as the ones inside the southeast severe UHI areas that were mainly related to extensive human activities, e.g., high-frequency railway traffic and industrial production. In general, buildings and impervious surfaces registered the highest mean LST of 44.18 ℃ and 43.17 ℃ (Fig. 2c), respectively. The mean LST of bare lands was 41.06 ℃. A large area of urban trees and grasslands located in northern urban areas (Fig. 1c) generated substantial cool islands (Fig. 2a) and had a relatively lower mean LST of 40.44 ℃ and 37.62 ℃, respectively. Water bodies registered the lowest average LST of 36.06 ℃.

3.2. Local cooling/warming effects of land cover types

The local cooling/warming effects of land cover types are regarded as the negative/positive response of LST* to a coverage increase of a particular land cover type while holding other types constant. It can readily be derived from the regression coefficients (Table 4). According to the results of the elastic net regression, all the land cover types significantly (at the 0.05 level) contribute to the local thermal environment except for bare lands. For every 10% coverage increase, water bodies, grasslands, and urban trees show different cooling effects that reduce the LST* by 0.72 ℃, 0.60 ℃ and 0.57 ℃, respectively. In contrast, buildings appear to have a strong warming effect and raise the LST* by 1.26 ℃, while impervious surfaces elevate the LST* by 0.23 ℃.

Compared to the elastic net regression, the multiple regression shows the same fitting accuracy (R^2 = 0.81, Table 4) and a slightly lower root mean squared error (RMSE) (0.922 ℃, Table 4). However, the coefficients severely inflate due to collinearity, and all coefficients are not statistically significant. For any of the land cover types, the absolute values of the coefficients obtained by the simple regression are greater than those obtained by the elastic net regression. Since only a single land cover type is considered, the simple regression results in worse model fitting and larger RMSE ranging from 1.17 ℃ to 2.11 ℃ (Table 4). In addition, by comparing the standard deviations of coefficients in Table 4, the elastic net regression provides more stable results than the simple regression. A similar comparison of standardized coefficients between the simple regression, multiple regression, and elastic net regression can be found in Table S3.

3.3. Does landscape configuration always have an effect?

To quantify the thermal contribution of landscape configuration, we detached the effect of configuration from the effect of composition at each FVC level. The net effect of vegetation aggregation represents different patterns at different FVC levels (Fig. 3). When FVC is below 40% (L1–3 in Fig. 3a–c), LST* significantly decreases as the aggregation of vegetation increases. Furthermore, an increasing slope of trend lines implies the aggregation cooling (shaded area with negative AE)

Table 3
Average land cover fractions (%) at each fractional vegetation cover (FVC) level.

FVC level	n	FVC (urban tree + grassland, %)	Average land cover fractions (%)					
			Water body	Urban tree	Grassland	Bare land	Impervious surface	Building
L1	61	[10, 20)	0.65	16.53	0.13	0.85	55.28	26.56
L2	115	[20, 30)	1.03	24.40	0.66	0.55	51.95	21.40
L3	38	[30, 40)	3.35	31.99	2.53	0.46	45.08	16.58
L4	26	[40, 50)	2.96	37.13	7.37	0.13	40.41	11.99
L5	15	> =50	5.73	49.56	11.94	0.68	26.56	5.53

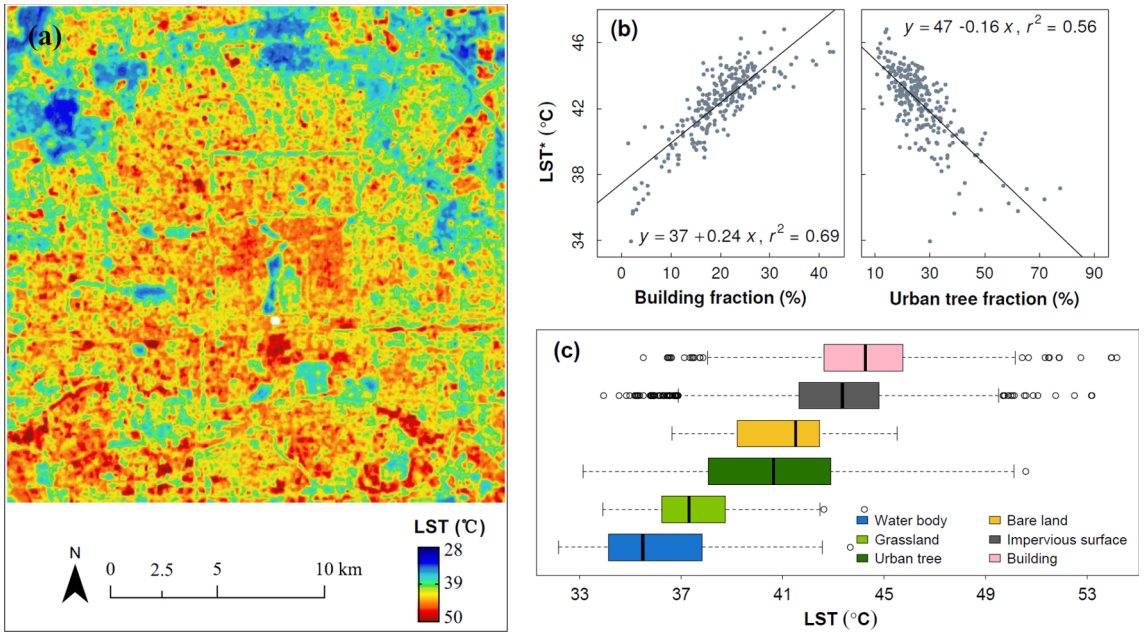

Fig. 2. Thermal environments in the Beijing metropolitan region. (a) LSTs in ℃ across the Beijing metropolitan region in the summer of 2017 derived from a Landsat 8 thermal image with a spatial resolution of 30 m. (b) Scatters for the local LST (LST*) vs. building/urban tree fraction. (c) Distribution of LSTs for different land cover types.

strengthens from low to high FVC. The maximum aggregation cooling could be observed ranging from approximately -1.0 ℃ (Fig. 3c) to -1.2 ℃ (Fig. 3a). However, when FVC is above 40% (L4–5 in Fig. 3d–e), most of the observations are scattered around the theoretical LST* line and a significant slope between LST*/AE and AI cannot be found. This implies that the aggregation cooling of vegetation becomes minor in the cases of high vegetation coverage.

The net effect of building aggregation is also dependent on composition. The distributions of building coverage at each FVC level are represented in Fig. S2. In the cases of mean building coverage of more than 15% (L1–3 in Fig. 4a–c), LST* significantly increases as buildings become aggregated. The warming effect of building aggregation (shaded area with positive AE) occurs when the ENN of buildings is less than 7.8 m, 10.2 m, and 11.3 m for the mean building coverage of above 25% (Fig. 4a), between 20% and 25% (Fig. 4b), and between 15% and 20%, respectively (Fig. 4c). The aggregation warming also strengthens as building coverage increases, indicated by an increasing slope of trend lines. The maximum warming is from 1.0 ℃ (Fig. 4c) to 1.3 ℃ (Fig. 4a). In low building coverage cases (L4–5 in Fig. 4d–e), the relationship between LST*/AE and ENN is not statistically significant, meaning that building aggregation has a limited effect when building coverage is low.

4. Discussion

4.1. Performance of the elastic net regression

In this study, the local cooling/warming effects of six urban land cover types were distinguished by modeling the relationship between LST* and landscape composition using elastic net regression, i.e., the changes in LST* response to a 1% coverage increase of a particular type (Table 4). Such effects are differentiated from pixel-based LST (Fig. 2c) by clarifying the direction of heat transfer and detaching the magnitude of thermal contributions from different land cover types. A number of studies have modeled the relationship between a single land cover (e.g., urban trees, buildings) and local LST based on the simple regression (Chen and Yu, 2017; Connors et al., 2013; Li et al., 2017; Simanjuntak et al., 2019). This approach is appropriate for simple land cover scenarios because local LST could be regulated by the most dominant land cover. Nonetheless, it might not be suitable for complex cases such as a metropolis where the local thermal environment is affected by several kinds of land cover types simultaneously.

This inadequacy could be illustrated by contrasting the model coefficients and fitting accuracy of the simple regression, multiple regression, and elastic net regression (Table 4). The simple regression for

Table 4
Comparison of model coefficients and fitting accuracy between the simple regression, multiple regression, and elastic net regression.

Land cover type	Simple regression			Multiple regression (R^2 = 0.81, RMSE = 0.922 ℃)	Elastic net regression (R^2 = 0.81, RMSE = 0.923 ℃)
	Coefficient ± S.D.	R^2	RMSE (℃)	Coefficient ± S.D.	Coefficient ± S.D.
Water body	−0.205 ± 0.0242***	0.22	1.861	17139.73 ± 34782	−0.0723 ± 0.00165**
Urban tree	−0.158 ± 0.00876***	0.56	1.392	17139.75 ± 34782	−0.0566 ± 0.000264***
Grassland	−0.217 ± 0.0228***	0.26	1.807	17139.75 ± 34782	−0.0603 ± 0.000550*
Bare land	0.00570 ± 0.0391	0.000084	2.106	17139.83 ± 34782	0.0141 ± 0.00181
Impervious surface	0.144 ± 0.0104***	0.43	1.587	17139.83 ± 34782	0.0225 ± 0.000279*
Building	0.244 ± 0.0103***	0.69	1.173	17139.94 ± 34782	0.126 ± 0.000288***

***Significant at the 0.001 level.
**Significant at the 0.01 level.
*Significant at the 0.05 level.

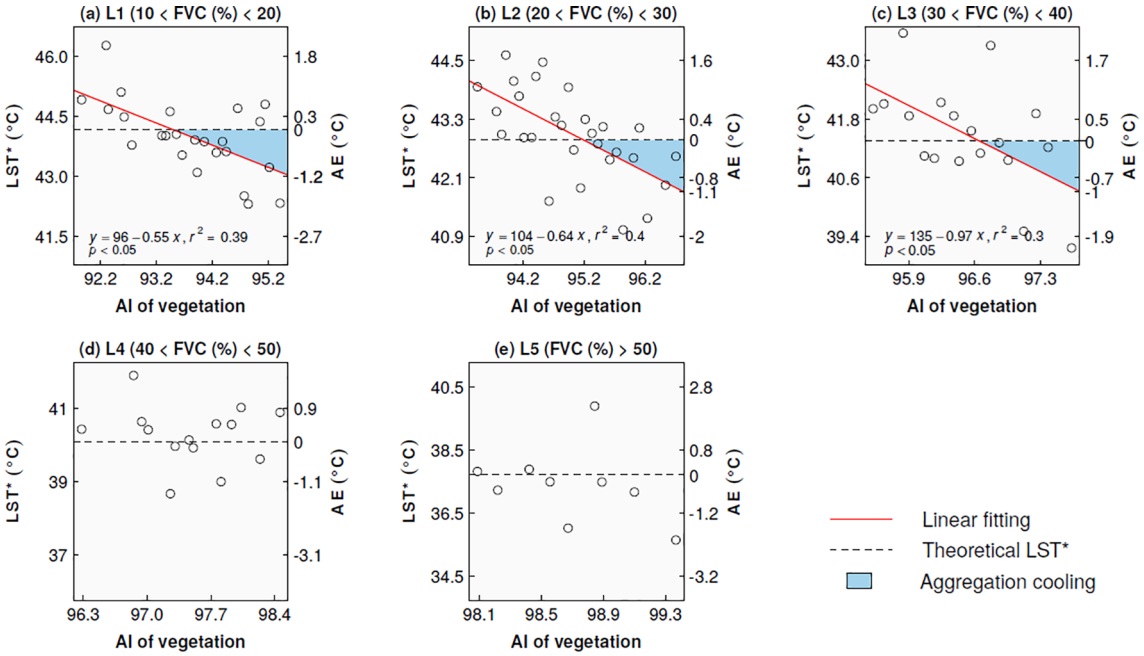

Fig. 3. Relationship between local LST (LST*)/aggregation effect (AE) and the aggregation index (AI) of vegetation at different fractional vegetation cover (FVC) levels. The solid red line is the linear fitting line. The dashed black line represents the theoretical average LST* at each FVC level. The shaded area in blue represents the aggregation cooling of vegetation. The relationship between LST*/AE and the AI of vegetation is not significant at the 0.05 level in the figures without a linear fitting line. (For interpretation of the references to colour in this figure legend, the reader is referred to the web version of this article.)

a single land cover type only partially explains the variance of LST*, although the urban tree (R^2 = 0.56) or building (R^2 = 0.67) fraction explains more than half. Compared to the elastic net regression, the cooling/warming effects are overestimated by the simple regression, for example, approximately 0.16 ℃ for grassland cooling or 0.12 ℃ for building warming. The multiple regression achieves a model fitting as good the elastic net regression and even smaller estimation errors. Nevertheless, the thermal contributions cannot be interpreted due to the inflated coefficients. In contrast, the elastic net regression addresses the structural collinearity intrinsic to multiple land covers and represents explicit cooling/warming effects without a loss of precision.

4.2. Factors affecting the thermal contribution

LULC changes could be the principal cause of LST variation. Most farmlands were converted to impervious surfaces from 1999 to 2010 in

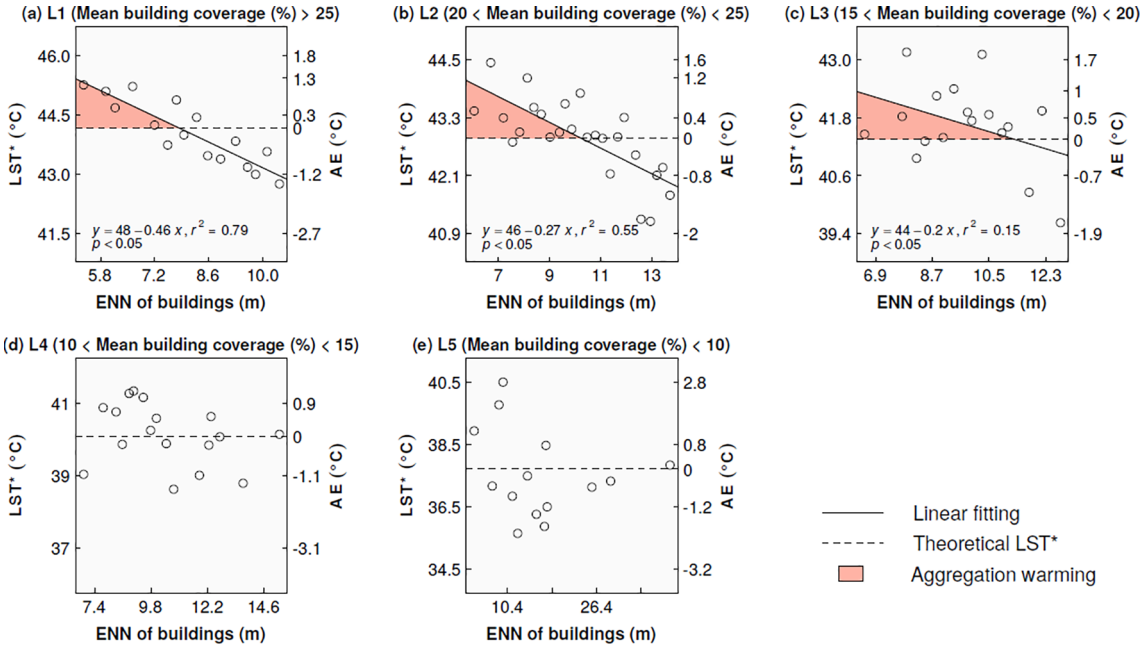

Fig. 4. Relationship between local LST (LST*)/aggregation effect (AE) and the Euclidean nearest-neighbor distance (ENN) of buildings at different fractional vegetation cover (FVC) levels. The solid black line is the linear fitting line. The dashed black line represents the theoretical average LST* at each FVC level. The shaded area in pink represents the aggregation warming of buildings. The relationship between LST*/AE and the ENN of buildings is not significant at the 0.05 level in the figures without a linear fitting line. (For interpretation of the references to colour in this figure legend, the reader is referred to the web version of this article.)

Beijing and a definite increase in LST due to such conversion was observed (Ding and Shi, 2013). A simulation study over the lower Himalayan region likewise indicated that increasing build-up areas and decreasing vegetation accompanied by urban expansion would lead to more than 50% of surface warming in the next 30 years (Ullah et al., 2019). The local cooling/warming effects of different land cover types identified in this study help to understand these processes. However, the processes could be affected by internal and external factors.

Trees reduce temperatures both through evapotranspiration and shading. Therefore, they are sometimes expected to have a higher cooling effect than grass. However, the evaporative cooling of trees inherently varies greatly between species due to different physiological traits (Rahman et al., 2015). This process in daily scale is driven by microclimate features including humidity, temperature, wind flow and by soil conditions in the long term (Chen et al., 2019; Gunawardena et al., 2017). The shading created by the tree canopy contributes to incoming solar radiation interception (Fahmy et al., 2010; Kotzen, 2003) and therefore provides additional cooling. However, such shading cooling largely depends on foliage density, tree height, and canopy geometry (Kotzen, 2003; Shahidan et al., 2012). Thus, various cooling effects of trees could be observed across cities, such as Guangzhou (0.30 ℃ for a 10% increase in coverage) (Hu and Jia, 2010), Hangzhou (0.41 ℃ for a 10% increase in coverage) (Sheng et al., 2015), megacities in Southeast Asia (ranging from 0.59 to 1.18 ℃ for a 10% increase in coverage) (Estoque et al., 2017) and that in our study (0.57 ℃ for a 10% increase in coverage, Table 4). A comparative study in the U.S. indicates the daytime cooling efficiency of trees in Phoenix was found to be much higher than that of grass but almost the same as that in Las Vegas (Myint et al., 2015).

Compared with trees, grass produces cooling mainly through evapotranspiration. According to (Rahman et al., 2011), trees have a more intensive evapotranspiration process than an equivalent area of grass. However, our results indicate that for a local urban area of 1440 m^2, the cooling effect of grass is comparable to that of trees (Table 4). This finding might be because the grasslands in Beijing, except for some grass in playing fields, are generally planted together with trees (Fig. 1c), hence leading to a synergistic cooling effect. Experimental work from southern Israel (Shashua-Bar et al., 2009) demonstrates that grass can provide greater cooling when shaded. However, due to the shallow roots, the cooling effect of grass is more easily affected by irrigation conditions than trees (Armson et al., 2012; Shashua-Bar et al., 2009). A modeling study from Manchester (Gill et al., 2013) also indicates that the evaporative cooling effect of grass would be reduced by more than 50% under a severe short-term drought.

For heat sources, buildings have a much stronger warming effect than impervious surfaces (Table 4). This result contradicts the findings of Zheng et al. (2014), according to which the composition and spatial pattern of buildings have a limited impact on LST while that of paved surfaces alter LST more intensely. This discrepancy might be because many roads in Beijing are partly shaded by the trees/buildings alongside roads (Xiao et al., 2008). Moreover, many rooftops in Beijing are dark-colored and thus retain a large amount of heat compared to the light-colored ones in Zheng's case. More importantly, the warming effect of buildings changes with building size, height and geometry as well as the distance between the building and other features.

Other factors including modeling approaches and land cover maps with different spatial resolutions also result in different thermal contribution assessments since such assessments are derived from landscape patterns, which are scale-dependent (Li, Zhou, & et al., 2013; Wu, 2004).

4.3. Interaction between composition and configuration

Urban thermal environments are mostly affected by landscape composition and configuration, both of which change as LULC changes associated with urbanization processes. A previous fine-scale study observed an increase in greenspace coverage as well as mean patch size in the Core Function Zone of Beijing (Fig. 1b) from 2005 to 2009 (Qian et al., 2015). It could be expected that this landscape transformation played a part in alleviating thermal stress in the inner city (Peng et al., 2016). The effect of configuration would be particularly important for highly urbanized metropolises due to the very limited amounts of land available for greening. Since a larger patch tends to be highly aggregated (Zheng et al., 2014), the effect of composition is easily confused with that of configuration. Therefore, we grouped observations by the FVC level (Table 3) to manifest the unmixed cooling/warming effect of vegetation/building aggregation.

The aggregation effect has been mentioned in previous studies (Estoque et al., 2017). However, we found that spatial aggregation interacts with the composition to affect local LST (Fig. 3, Fig. 4). Such interactions are represented as (1) different maximum cooling/warming observed for different FVC levels, ranging from -1.0 to -1.2 ℃ for vegetation cooling and 1.0 to 1.3 ℃ for building warming; (2) different aggregation thresholds for achieving aggregation cooling/warming at different FVC levels; and (3) different composition requirements for aggregation cooling/warming (less than 40% vegetation coverage for aggregation cooling and more than 15% building coverage for aggregation warming).

Given the complexity of energy exchange in the urban system, whether an aggregated or dispersed arrangement achieves lower LST remains uncertain across various urban morphologies, e.g., opposite arguments were made by Zhang et al. (2009) and Zhou et al. (2011). One possible reason for the aggregation cooling might be that an aggregated arrangement locally increases leaf area index, thus resulting in a more concentrated evapotranspiration (Murakami et al., 2000; Toda et al., 2010). This enhancement substantially reduces the LST of tree canopies and helps to form cooling islands. However, such an effect is not significant as the tree coverage exceeds a certain threshold (40% in our case, Fig. 3d–e). Moreover, the spatial arrangement also affects local LST through different energy exchanges between land cover features (Forman, 2014). Vegetation canopies modify surface roughness and background wind flow to generate mechanical turbulence, thereby altering heat convection (Gunawardena et al., 2017). In the Beijing metropolitan region, tree species are very abundant, including 45 arbor species and 33 shrub species found in sample plots (Yang et al., 2005). Tree clusters with heterogeneous canopies might facilitate the energy flow between vegetation and its surrounding features, resulting in an aggregation cooling (Ren et al., 2015). Nevertheless, more field or simulation-based measurements are needed to further support such a claim.

Significant building aggregation warming is identified (Fig. 4). Building clusters warm surrounding areas by increasing shortwave radiation and decreasing longwave emission due to the fact that high buildings change the urban canyon geometry (Bottyán and Unger, 2003). This blockage effect is exacerbated by building aggregation. In our case, the aggregation threshold on average is approximately 10 m (Fig. 4a–c), below which aggregation warming occurs. However, such aggregation warming along with the blockage effect seems to require a particular building coverage ($> 15\%$, Fig. 4).

Buildings may also have a cooling effect (Myint et al., 2013). High building clusters project even more substantial shading than tree canopies, thereby providing cooling to objects nearby. Thus, whether buildings cool or warm surroundings depends to a certain extent on the net effect of shading cooling and blockage warming.

4.4. Management implications

This study assesses the thermal contributions of six land cover types in the Beijing metropolitan region. Despite very limited coverage (Fig. 1c), water bodies were found to be the most effective type at reducing local LST. Thus, increasing the area of water bodies, e.g., lakes, rivers, or other open water can substantially alleviate UHIs and should

be highly encouraged. Both trees and grass can effectively cool surroundings, and the cooling effects of the two were found to be parallel. Thus, urban designers could replace grass with trees in locations where the irrigation conditions are inappropriate or where footfall occurs frequently.

In landscape planning, the requirements for spatial pattern varies based on different design needs. From the perspective of thermal environment modification, the spatial pattern of vegetation/buildings might be more flexible when vegetation/building coverage is more/less than 40%/15%. In contrast, aggregated arrangements of vegetation might be desired for additional aggregation cooling when vegetation coverage is below 40%. When building coverage is above 15%, planners should be cautious about the distance between buildings and avoid distances of less than 10 m when possible. All of these implications might provide insights into urban expansion or new town planning.

4.5. Limitations and future works

The study has several limitations in terms of data, method applicability, and other aspects. Using only one LST image acquired on hot summer days to manifest the thermal contributions of various land cover types might be insufficient because their thermal processes exhibit diurnal variations that change with weather conditions. For instance, a more substantial cooling effect of trees was observed in U.S. cities during heat waves (Wang et al., 2019). Furthermore, our assessments highlight the combined effect of composition and configuration. More detailed works that take tree species, building height/structure, and anthropogenic heats (Buyantuyev and Wu, 2010; Tran et al., 2006) into consideration are desirable in the future. In addition, the findings in this study were empirically estimated and need to be further explained by mechanical models.

5. Conclusions

The imbalance of the urban thermal environment is a severe consequence of urbanization. Perceiving the relationship between land cover and the urban thermal environment is therefore crucial for UHI mitigation. In our work, we used elastic net regularized regression to assess the thermal contributions of six urban land cover types from the perspectives of landscape composition and configuration. We found the followings: (1) Different land cover types have varying impacts on LST and only considering a single land cover in complex landscapes such as metropolises might result in biased thermal contribution assessments. (2) Compared to OLS-based regressions, elastic net regression could be more appropriate for modeling the LST-composition relation by accounting for the perfect collinearity among multiple land covers. (3) In the Beijing metropolitan region, buildings contribute the most to the UHI effect. The warming effect of the building is much higher than that of the impervious surface. It elevates the mean LST of a 1440 m × 1440 m local area by approximately 1.26 ℃ for a 10% increase in coverage. (4) For an equivalent coverage increase, water bodies, grasslands and urban trees could reduce the local LST by approximately 0.72 ℃, 0.60 ℃ and 0.57 ℃, respectively. (5) Landscape configuration interacts with the composition to affect local LST. In our case, the aggregation cooling of vegetation only takes effect when the local vegetation coverage is less than 40%, ranging from -1.0 to -1.2 ℃. Building aggregation plays a role in local warming of 1.0 to 1.3 ℃ only when the building coverage is more than 15%.

Overall, increasing the area of water bodies, trees, and grass in Beijing can substantially alleviate UHIs. The urban thermal environment also benefits from optimizing spatial configuration, but we highlight that such benefits might be based on landscape composition. Clustering green patches for low green cover areas gains additional aggregation cooling while dispersing building clusters for high building cover areas could alleviate aggregation warming. These findings assist urban planners in developing UHI mitigation strategies and landscape planning.

CRediT authorship contribution statement

Jiacheng Zhao: Conceptualization, Methodology, Software, Formal analysis, Investigation, Writing - original draft, Writing - review & editing, Visualization. **Xiang Zhao:** Conceptualization, Methodology, Formal analysis, Resources, Writing - review & editing, Project administration, Funding acquisition. **Shunlin Liang:** Resources, Supervision, Project administration. **Tao Zhou:** Methodology, Formal analysis, Resources, Writing - review & editing. **Xiaozheng Du:** Investigation, Writing - review & editing, Visualization. **Peipei Xu:** Investigation, Writing - review & editing. **Donghai Wu:** Methodology, Formal analysis, Investigation, Writing - review & editing.

Acknowledgements

This study was supported by the National Key Research and Development Program of China (No. 2016YFA0600103, No. 2016YFB0501404). We are grateful to the three anonymous reviewers and associate editor for their valuable comments on the manuscript. We appreciate the China Center for Resources Satellite Data and Application (CRESDA, http://www.cresda.com/EN/) for providing the GF-2 data.

Appendix A. Supplementary data

Supplementary data to this article can be found online at https://doi.org/10.1016/j.landurbplan.2020.103927.

References

Abdullah, A. Y. M., Masrur, A., Adnan, M. S. G., Baky, M., Al, A., Hassan, Q. K., & Dewan, A. (2019). Spatio-temporal patterns of land use/land cover change in the heterogeneous coastal region of Bangladesh between 1990 and 2017. *Remote Sensing, 11*(7), 790. https://doi.org/10.3390/rs11070790.

Anderson, G. B., & Bell, M. L. (2010). Heat waves in the United States: Mortality risk during heat waves and effect modification by heat wave characteristics in 43 US communities. *Environmental Health Perspectives, 119*(2), 210–218. https://doi.org/10.1289/ehp.1002313.

Armson, D., Stringer, P., & Ennos, A. (2012). The effect of tree shade and grass on surface and globe temperatures in an urban area. *Urban Forestry & Urban Greening, 11*(3), 245–255. https://doi.org/10.1016/j.ufug.2012.05.002.

Beijing Municipal Bureau Statistics (2018). Beijing Statistical Yearbook 2018. Available at http://nj.tjj.beijing.gov.cn/nj/main/2018-tjnj/zk/indexch.htm.

Bottyán, Z., & Unger, J. (2003). A multiple linear statistical model for estimating the mean maximum urban heat island. *Theoretical and Applied Climatology, 75*(3–4), 233–243. https://doi.org/10.1007/s00704-003-0735-7.

Breiman, L. (2001). Random forests. *Machine Learning, 45*(1), 5–32. https://doi.org/10.1023/A:1010933404324.

Buyantuyev, A., & Wu, J. (2010). Urban heat islands and landscape heterogeneity: Linking spatiotemporal variations in surface temperatures to land-cover and socioeconomic patterns. *Landscape Ecology, 25*(1), 17–33. https://doi.org/10.1007/s10980-009-9402-4.

Candia, J., & Tsang, J. S. (2019). eNetXplorer: An R package for the quantitative exploration of elastic net families for generalized linear models. *BMC Bioinformatics, 20*(1), 189. https://doi.org/10.1186/s12859-019-2778-5.

Chakraborty, T., & Lee, X. (2019). A simplified urban-extent algorithm to characterize surface urban heat islands on a global scale and examine vegetation control on their spatiotemporal variability. *International journal of applied earth observation and geoinformation, 74*, 269–280. https://doi.org/10.1016/j.jag.2018.09.015.

Chen, X., Chen, J., Jia, X., & Wu, J. (2010). Impact of collinearity on linear and nonlinear spectral mixture analysis. In 2010 2nd workshop on hyperspectral image and signal processing: evolution in remote sensing (pp. 1–4). Reykjavik, Iceland: IEEE. doi:10.1109/WHISPERS.2010.5594918.

Chen, X., Zhao, P., Hu, Y., Ouyang, L., Zhu, L., & Ni, G. (2019). Canopy transpiration and its cooling effect of three urban tree species in a subtropical city-Guangzhou, China. *Urban Forestry & Urban Greening, 43*, Article 126368. https://doi.org/10.1016/j.ufug.2019.126368.

Chen, Y., & Yu, S. (2017). Impacts of urban landscape patterns on urban thermal variations in Guangzhou, China. *International journal of applied earth observation and geoinformation, 54*, 65–71. https://doi.org/10.1016/j.jag.2016.09.007.

Chun, B., & Guldmann, J.-M. (2014). Spatial statistical analysis and simulation of the urban heat island in high-density central cities. *Landscape and Urban Planning, 125*, 76–88. https://doi.org/10.1016/j.landurbplan.2014.01.016.

Connors, J. P., Galletti, C. S., & Chow, W. T. (2013). Landscape configuration and urban heat island effects: Assessing the relationship between landscape characteristics and land surface temperature in Phoenix, Arizona. *Landscape Ecology, 28*(2), 271–283.

https://doi.org/10.1007/s10980-012-9833-1.
Deilami, K., Kamruzzaman, M., & Liu, Y. (2018). Urban heat island effect: A systematic review of spatio-temporal factors, data, methods, and mitigation measures. *International journal of applied earth observation and geoinformation, 67*, 30–42. https://doi.org/10.1016/j.jag.2017.12.009.
Ding, H., & Shi, W. (2013). Land-use/land-cover change and its influence on surface temperature: A case study in Beijing City. *International Journal of Remote Sensing, 34*(15), 5503–5517. https://doi.org/10.3390/rs11070790.
Du, S., Xiong, Z., Wang, Y.-C., & Guo, L. (2016). Quantifying the multilevel effects of landscape composition and configuration on land surface temperature. *Remote Sensing of Environment, 178*, 84–92. https://doi.org/10.1016/j.rse.2016.02.063.
Duncan, J., Boruff, B., Saunders, A., Sun, Q., Hurley, J., & Amati, M. (2019). Turning down the heat: An enhanced understanding of the relationship between urban vegetation and surface temperature at the city scale. *Science of the Total Environment, 656*, 118–128. https://doi.org/10.1016/j.scitotenv.2018.11.223.
Estoque, R. C., Murayama, Y., & Myint, S. W. (2017). Effects of landscape composition and pattern on land surface temperature: An urban heat island study in the megacities of Southeast Asia. *Science of the Total Environment, 577*, 349–359. https://doi.org/10.1016/j.scitotenv.2016.10.195.
Fahmy, M., Sharples, S., & Yahiya, M. (2010). LAI based trees selection for mid latitude urban developments: A microclimatic study in Cairo, Egypt. *Building and Environment, 45*(2), 345–357. https://doi.org/10.1016/j.buildenv.2009.06.014.
Foody, G. M. (2002). Status of land cover classification accuracy assessment. *Remote Sensing of Environment, 80*(1), 185–201. https://doi.org/10.1016/S0034-4257(01)00295-4.
Forman, R. T. (2014). Land Mosaics: The ecology of landscapes and regions (1995). In The ecological design and planning reader (pp. 217–234). Washington, DC: Island Press.
Fotheringham, A., Brunsdon, C., & Charlton, M. (2002). Geographically weighted regression: the analysis of spatially varying relationships. Chichester: Wiley.
Giles, D. M., Sinyuk, A., Sorokin, M. G., Schafer, J. S., Smirnov, A., Slutsker, I., ... Campbell, J. R. (2019). Advancements in the Aerosol Robotic Network (AERONET) Version 3 database–automated near-real-time quality control algorithm with improved cloud screening for Sun photometer aerosol optical depth (AOD) measurements. *Atmospheric Measurement Techniques, 12*(1), 169–209. https://doi.org/10.5194/amt-12-169-2019.
Gill, S., Rahman, M., Handley, J., & Ennos, A. (2013). Modelling water stress to urban amenity grass in Manchester UK under climate change and its potential impacts in reducing urban cooling. *Urban Forestry & Urban Greening, 12*(3), 350–358. https://doi.org/10.1016/j.ufug.2013.03.005.
Graham, M. H. (2003). Confronting multicollinearity in ecological multiple regression. *Ecology, 84*(11), 2809–2815. https://doi.org/10.1890/02-3114.
Grimm, N. B., Faeth, S. H., Golubiewski, N. E., Redman, C. L., Wu, J., Bai, X., & Briggs, J. M. (2008). Global change and the ecology of cities. *Science, 319*(5864), 756–760. https://doi.org/10.1126/science.1150195.
Gros, A., Bozonnet, E., Inard, C., & Musy, M. (2016). Simulation tools to assess microclimate and building energy–A case study on the design of a new district. *Energy and Buildings, 114*, 112–122. https://doi.org/10.1016/j.enbuild.2015.06.032.
Gunawardena, K., Wells, M., & Kershaw, T. (2017). Utilising green and bluespace to mitigate urban heat island intensity. *Science of the Total Environment, 584*, 1040–1055. https://doi.org/10.1016/j.scitotenv.2017.01.158.
Haashemi, S., Weng, Q., Darvishi, A., & Alavipanah, S. K. (2016). Seasonal variations of the surface urban heat island in a semi-arid city. *Remote Sensing, 8*(4), 352. https://doi.org/10.3390/rs8040352.
Hamoodi, M. N., Corner, R., & Dewan, A. (2019). Thermophysical behaviour of LULC surfaces and their effect on the urban thermal environment. *Journal of Spatial Science, 64*(1), 111–130. https://doi.org/10.1080/14498596.2017.1386598.
Han, H., Yang, C., & Song, J. (2015). Scenario simulation and the prediction of land use and land cover change in Beijing, China. *Sustainability, 7*(4), 4260–4279. https://doi.org/10.3390/su7044260.
Hao, P., Niu, Z., Zhan, Y., Wu, Y., Wang, L., & Liu, Y. (2016). Spatiotemporal changes of urban impervious surface area and land surface temperature in Beijing from 1990 to 2014. *GIScience & Remote Sensing, 53*(1), 63–84. https://doi.org/10.1080/15481603.2015.1095471.
Hu, Y., & Jia, G. (2010). Influence of land use change on urban heat island derived from multi-sensor data. *International Journal of Climatology, 30*(9), 1382–1395. https://doi.org/10.1002/joc.1984.
Huang, K., Yi, C., Wu, D., Zhou, T., Zhao, X., Blanford, W. J., ... Li, Z. (2015). Tipping point of a conifer forest ecosystem under severe drought. *Environmental Research Letters, 10*(2), Article 024011. https://doi.org/10.1088/1748-9326/10/2/024011.
Iping, A., Kidston-Lattari, J., Simpson-Young, A., Duncan, E., & McManus, P. (2019). (Re) presenting urban heat islands in Australian cities: A study of media reporting and implications for urban heat and climate change debates. *Urban Climate, 27*, 420–429. https://doi.org/10.1016/j.uclim.2018.12.014.
Jaeger, J. A., Bertiller, R., Schwick, C., & Kienast, F. (2010). Suitability criteria for measures of urban sprawl. *Ecological indicators, 10*(2), 397–406. https://doi.org/10.1016/j.ecolind.2009.07.007.
Jenerette, G. D., Harlan, S. L., Buyantuev, A., Stefanov, W. L., Declet-Barreto, J., Ruddell, B. L., ... Li, X. (2016). Micro-scale urban surface temperatures are related to land-cover features and residential heat related health impacts in Phoenix, AZ USA. *Landscape Ecology, 31*(4), 745–760. https://doi.org/10.1007/s10980-015-0284-3.
Jiménez-Muñoz, J. C., Cristóbal, J., Sobrino, J. A., Sòria, G., Ninyerola, M., & Pons, X. (2008). Revision of the single-channel algorithm for land surface temperature retrieval from Landsat thermal-infrared data. *IEEE Transactions on geoscience and remote sensing, 47*(1), 339–349. https://doi.org/10.1109/TGRS.2008.2007125.
Jiménez-Muñoz, J. C., Sobrino, J. A., Skoković, D., Mattar, C., & Cristóbal, J. (2014). Land surface temperature retrieval methods from Landsat-8 thermal infrared sensor data. *IEEE Geoscience and Remote Sensing Letters, 11*(10), 1840–1843. https://doi.org/10.1109/LGRS.2014.2312032.
Kmita, M., Fraudeau, N., Hérault, Y., & Duboule, D. (2002). Serial deletions and duplications suggest a mechanism for the collinearity of Hoxd genes in limbs. *Nature, 420*(6912), 145. https://doi.org/10.1038/nature01189.
Kotzen, B. (2003). An investigation of shade under six different tree species of the Negev desert towards their potential use for enhancing micro-climatic conditions in landscape architectural development. *Journal of Arid Environments, 55*(2), 231–274. https://doi.org/10.1016/S0140-1963(03)00030-2.
Lai, J., Zhan, W., Huang, F., Voogt, J., Bechtel, B., Allen, M., ... Du, P. (2018). Identification of typical diurnal patterns for clear-sky climatology of surface urban heat islands. *Remote Sensing of Environment, 217*, 203–220. https://doi.org/10.1016/j.rse.2018.08.021.
Lenters, V., Portengen, L., Rignell-Hydbom, A., Jönsson, B. A., Lindh, C. H., Piersma, A. H., ... Rylander, L. (2015). Prenatal phthalate, perfluoroalkyl acid, and organochlorine exposures and term birth weight in three birth cohorts: Multi-pollutant models based on elastic net regression. *Environmental Health Perspectives, 124*(3), 365–372. https://doi.org/10.1289/ehp.1408933.
Li, H., Meier, F., Lee, X., Chakraborty, T., Liu, J., Schaap, M., & Sodoudi, S. (2018). Interaction between urban heat island and urban pollution island during summer in Berlin. *Science of the Total Environment, 636*, 818–828. https://doi.org/10.1016/j.scitotenv.2018.04.254.
Li, H., Zhou, Y., Li, X., Meng, L., Wang, X., Wu, S., & Sodoudi, S. (2018). A new method to quantify surface urban heat island intensity. *Science of the Total Environment, 624*, 262–272. https://doi.org/10.1016/j.scitotenv.2017.11.360.
Li, J., Song, C., Cao, L., Zhu, F., Meng, X., & Wu, J. (2011). Impacts of landscape structure on surface urban heat islands: A case study of Shanghai, China. *Remote Sensing of Environment, 115*(12), 3249–3263. https://doi.org/10.1016/j.rse.2011.07.008.
Li, W., Cao, Q., Lang, K., & Wu, J. (2017). Linking potential heat source and sink to urban heat island: Heterogeneous effects of landscape pattern on land surface temperature. *Science of the Total Environment, 586*, 457–465. https://doi.org/10.1016/j.scitotenv.2017.01.191.
Li, X., Li, W., Middel, A., Harlan, S., Brazel, A., & Turner Ii, B. (2016). Remote sensing of the surface urban heat island and land architecture in Phoenix, Arizona: Combined effects of land composition and configuration and cadastral–demographic–economic factors. *Remote Sensing of Environment, 174*, 233–243. https://doi.org/10.1016/j.rse.2015.12.022.
Li, X., Zhou, W., & Ouyang, Z. (2013). Relationship between land surface temperature and spatial pattern of greenspace: What are the effects of spatial resolution? *Landscape and Urban Planning, 114*, 1–8. https://doi.org/10.1016/j.landurbplan.2013.02.005.
Li, X., Zhou, W., Ouyang, Z., Xu, W., & Zheng, H. (2012). Spatial pattern of greenspace affects land surface temperature: Evidence from the heavily urbanized Beijing metropolitan area, China. *Landscape Ecology, 27*(6), 887–898. https://doi.org/10.1007/s10980-012-9731-6.
Li, Z.-L., Tang, B.-H., Wu, H., Ren, H., Yan, G., Wan, Z., ... Sobrino, J. A. (2013). Satellite-derived land surface temperature: Current status and perspectives. *Remote Sensing of Environment, 131*, 14–37. https://doi.org/10.1016/j.rse.2012.12.008.
Lu, D., & Weng, Q. (2007). A survey of image classification methods and techniques for improving classification performance. *International Journal of Remote Sensing, 28*(5), 823–870. https://doi.org/10.1080/01431160600746456.
Ma, Q., Wu, J., & He, C. (2016). A hierarchical analysis of the relationship between urban impervious surfaces and land surface temperatures: Spatial scale dependence, temporal variations, and bioclimatic modulation. *Landscape Ecology, 31*(5), 1139–1153. https://doi.org/10.1007/s10980-016-0356-z.
Maimaitiyiming, M., Ghulam, A., Tiyip, T., Pla, F., Latorre-Carmona, P., Halik, Ü., ... Caetano, M. (2014). Effects of green space spatial pattern on land surface temperature: Implications for sustainable urban planning and climate change adaptation. *ISPRS Journal of Photogrammetry and Remote Sensing, 89*, 59–66. https://doi.org/10.1016/j.isprsjprs.2013.12.010.
Malakar, N. K., Hulley, G. C., Hook, S. J., Laraby, K., Cook, M., & Schott, J. R. (2018). An operational land surface temperature product for Landsat thermal data: Methodology and validation. *IEEE Transactions on geoscience and remote sensing, 56*(10), 5717–5735. https://doi.org/10.1109/TGRS.2018.2824828.
Manoli, G., Fatichi, S., Schläpfer, M., Yu, K., Crowther, T. W., Meili, N., ... Bou-Zeid, E. (2019). Magnitude of urban heat islands largely explained by climate and population. *Nature, 573*(7772), 55–60. https://doi.org/10.1038/s41586-019-1512-9.
Mattar, C., Durán-Alarcón, C., Jiménez-Muñoz, J. C., Santamaría-Artigas, A., Olivera-Guerra, L., & Sobrino, J. A. (2015). Global atmospheric profiles from reanalysis information (GAPRI): A new database for earth surface temperature retrieval. *International Journal of Remote Sensing, 36*(19–20), 5045–5060. https://doi.org/10.1080/01431161.2015.1054965.
McGarigal, K., & Marks, B. J. (1995). Spatial pattern analysis program for quantifying landscape structure. Gen. Tech. Rep. PNW-GTR-351. US Department of Agriculture, Forest Service, Pacific Northwest Research Station, pp. 1–122.
Miles, V., & Esau, I. (2017). Seasonal and spatial characteristics of urban heat islands (UHIs) in northern West Siberian cities. *Remote Sensing, 9*(10), 989. https://doi.org/10.3390/rs9100989.
Montanaro, M., Gerace, A., Lunsford, A., & Reuter, D. (2014). Stray light artifacts in imagery from the Landsat 8 Thermal Infrared Sensor. *Remote Sensing, 6*(11), 10435–10456. https://doi.org/10.3390/rs61110435.
Mora, C., Dousset, B., Caldwell, I. R., Powell, F. E., Geronimo, R. C., Bielecki, C. R., ... Louis, L. V. (2017). Global risk of deadly heat. *Nature Climate Change, 7*(7), 501–506. https://doi.org/10.1038/nclimate3322.
Murakami, S., Tsuboyama, Y., Shimizu, T., Fujieda, M., & Noguchi, S. (2000). Variation of evapotranspiration with stand age and climate in a small Japanese forested catchment. *Journal of Hydrology, 227*(1–4), 114–127. https://doi.org/10.1016/S0022-1694(99)00175-4.
Myint, S. W., Gober, P., Brazel, A., Grossman-Clarke, S., & Weng, Q. (2011). Per-pixel vs. object-based classification of urban land cover extraction using high spatial resolution imagery. *Remote Sensing of Environment, 115*(5), 1145–1161. https://doi.org/10.1016/j.rse.2010.12.017.
Myint, S. W., Wentz, E. A., Brazel, A. J., & Quattrochi, D. A. (2013). The impact of distinct anthropogenic and vegetation features on urban warming. *Landscape Ecology, 28*(5), 959–978. https://doi.org/10.1007/s10980-013-9868-y.

Myint, S. W., Zheng, B., Talen, E., Fan, C., Kaplan, S., Middel, A., ... Brazel, A. (2015). Does the spatial arrangement of urban landscape matter? Examples of urban warming and cooling in Phoenix and Las Vegas. *Ecosystem Health and Sustainability, 1*(4), 1–15. https://doi.org/10.1890/EHS14-0028.1.

O'Malley, C., Piroozfar, P., Farr, E. R., & Pomponi, F. (2015). Urban Heat Island (UHI) mitigating strategies: A case-based comparative analysis. *Sustainable Cities and Society, 19*, 222–235. https://doi.org/10.1016/j.scs.2015.05.009.

Ostro, B. D., Roth, L. A., Green, R. S., & Basu, R. (2009). Estimating the mortality effect of the July 2006 California heat wave. *Environmental Research, 109*(5), 614–619. https://doi.org/10.1016/j.envres.2009.03.010.

Palme, M., Inostroza, L., Villacreses, G., Lobato-Cordero, A., & Carrasco, C. (2017). From urban climate to energy consumption. Enhancing building performance simulation by including the urban heat island effect. *Energy and Buildings, 145*, 107–120. https://doi.org/10.1016/j.enbuild.2017.03.069.

Parkin, I. A., Lydiate, D., & Trick, M. (2002). Assessing the level of collinearity between Arabidopsis thaliana and Brassica napus for A. thaliana chromosome 5. *Genome, 45*(2), 356–366. https://doi.org/10.1139/g01-160.

Parsaee, M., Joybari, M. M., Mirzaei, P. A., & Haghighat, F. (2019). Urban heat island, urban climate maps and urban development policies and action plans. *Environmental Technology & Innovation, 100341*. https://doi.org/10.1016/j.eti.2019.100341.

Peng, J., Xie, P., Liu, Y., & Ma, J. (2016). Urban thermal environment dynamics and associated landscape pattern factors: A case study in the Beijing metropolitan region. *Remote Sensing of Environment, 173*, 145–155. https://doi.org/10.1016/j.rse.2015.11.027.

Peng, S., Piao, S., Ciais, P., Friedlingstein, P., Ottle, C., Bréon, F. o.-M., Nan, H., Zhou, L., & Myneni, R. B. (2012). Surface urban heat island across 419 global big cities. Environmental Science & Technology 46(2), 696–703. https://doi.org/10.1021/es2030438.

Qaid, A., Lamit, H. B., Ossen, D. R., & Shahminan, R. N. R. (2016). Urban heat island and thermal comfort conditions at micro-climate scale in a tropical planned city. *Energy and Buildings, 133*, 577–595. https://doi.org/10.1016/j.enbuild.2016.10.006.

Qian, Y., Zhou, W., Yu, W., & Pickett, S. T. (2015). Quantifying spatiotemporal pattern of urban greenspace: New insights from high resolution data. *Landscape Ecology, 30*(7), 1165–1173. https://doi.org/10.1007/s10980-015-0195-3.

Rahman, M., Armson, D., & Ennos, A. (2015). A comparison of the growth and cooling effectiveness of five commonly planted urban tree species. *Urban Ecosystems, 18*(2), 371–389. https://doi.org/10.1007/s11252-014-0407-7.

Rahman, M., Smith, J., Stringer, P., & Ennos, A. (2011). Effect of rooting conditions on the growth and cooling ability of Pyrus calleryana. *Urban Forestry & Urban Greening, 10*(3), 185–192. https://doi.org/10.1016/j.ufug.2011.05.003.

Rajagopalan, P., Lim, K. C., & Jamei, E. (2014). Urban heat island and wind flow characteristics of a tropical city. *Solar Energy, 107*, 159–170. https://doi.org/10.1016/j.solener.2014.05.042.

Razzaghmanesh, M., Beecham, S., & Salemi, T. (2016). The role of green roofs in mitigating Urban Heat Island effects in the metropolitan area of Adelaide, South Australia. *Urban Forestry & Urban Greening, 15*, 89–102. https://doi.org/10.1016/j.ufug.2015.11.013.

Ren, Z., Zheng, H., He, X., Zhang, D., & Yu, X. (2015). Estimation of the relationship between urban vegetation configuration and land surface temperature with remote sensing. *Journal of the Indian Society of Remote Sensing, 43*(1), 89–100. https://doi.org/10.1007/s12524-014-0373-9.

Rodriguez-Galiano, V. F., Ghimire, B., Rogan, J., Chica-Olmo, M., & Rigol-Sanchez, J. P. (2012). An assessment of the effectiveness of a random forest classifier for land-cover classification. *ISPRS Journal of Photogrammetry and Remote Sensing, 67*, 93–104. https://doi.org/10.1016/j.isprsjprs.2011.11.002.

Santamouris, M., Cartalis, C., Synnefa, A., & Kolokotsa, D. (2015). On the impact of urban heat island and global warming on the power demand and electricity consumption of buildings—A review. *Energy and Buildings, 98*, 119–124. https://doi.org/10.1016/j.enbuild.2014.09.052.

Seto, K. C., Güneralp, B., & Hutyra, L. R. (2012). Global forecasts of urban expansion to 2030 and direct impacts on biodiversity and carbon pools. *Proceedings of the National Academy of Sciences, 109*(40), 16083–16088. https://doi.org/10.1073/pnas.1211658109.

Shahidan, M. F., Jones, P. J., Gwilliam, J., & Salleh, E. (2012). An evaluation of outdoor and building environment cooling achieved through combination modification of trees with ground materials. *Building and Environment, 58*, 245–257. https://doi.org/10.1016/j.buildenv.2012.07.012.

Shashua-Bar, L., Pearlmutter, D., & Erell, E. (2009). The cooling efficiency of urban landscape strategies in a hot dry climate. *Landscape and Urban Planning, 92*(3–4), 179–186. https://doi.org/10.1016/j.landurbplan.2009.04.005.

Shastri, H., Barik, B., Ghosh, S., Venkataraman, C., & Sadavarte, P. (2017). Flip flop of day-night and summer-winter surface urban heat island intensity in India. *Scientific Reports, 7*, 1–8. https://doi.org/10.1038/srep40178.

Sheng, L., Lu, D., & Huang, J. (2015). Impacts of land-cover types on an urban heat island in Hangzhou, China. *International Journal of Remote Sensing, 36*(6), 1584–1603. https://doi.org/10.1080/01431161.2015.1019016.

Shirani-Bidabadi, N., Nasrabadi, T., Faryadi, S., Larijani, A., & Roodposhti, M. S. (2019). Evaluating the spatial distribution and the intensity of urban heat island using remote sensing, case study of Isfahan city in Iran. *Sustainable Cities and Society, 45*, 686–692. https://doi.org/10.1016/j.scs.2018.12.005.

Simanjuntak, R. M., Kuffer, M., & Reckien, D. (2019). Object-based image analysis to map local climate zones: The case of Bandung, Indonesia. *Applied Geography, 106*, 108–121. https://doi.org/10.1016/j.apgeog.2019.04.001.

Song, J., Du, S., Feng, X., & Guo, L. (2014). The relationships between landscape compositions and land surface temperature: Quantifying their resolution sensitivity with spatial regression models. *Landscape and Urban Planning, 123*, 145–157. https://doi.org/10.1016/j.landurbplan.2013.11.014.

Streutker, D. R. (2003). Satellite-measured growth of the urban heat island of Houston, Texas. *Remote Sensing of Environment, 85*(3), 282–289. https://doi.org/10.1016/S0034-4257(03)00007-5.

Sun, W., Chen, B., & Messinger, D. (2014). Nearest-neighbor diffusion-based pan-sharpening algorithm for spectral images. *Optical Engineering, 53*(1), 1–11. https://doi.org/10.1117/1.OE.53.1.013107.

Taylor, J., Wilkinson, P., Davies, M., Armstrong, B., Chalabi, Z., Mavrogianni, A., ... Bohnenstengel, S. I. (2015). Mapping the effects of urban heat island, housing, and age on excess heat-related mortality in London. *Urban Climate, 14*, 517–528. https://doi.org/10.1016/j.uclim.2015.08.001.

The People's Government of Beijing Municipality (2005). Beijing General Planning (2004–2020).

The People's Government of Beijing Municipality (2006). Beijing Outline of the Eleventh Five-Year Program for National Economic and Social Development (2006–2010).

Toda, M., Yokozawa, M., Emori, S., & Hara, T. (2010). More asymmetric tree competition brings about more evapotranspiration and less runoff from the forest ecosystems: A simulation study. *Ecological Modelling, 221*(24), 2887–2898. https://doi.org/10.1016/j.ecolmodel.2010.08.025.

Tran, H., Uchihama, D., Ochi, S., & Yasuoka, Y. (2006). Assessment with satellite data of the urban heat island effects in Asian mega cities. *International journal of applied earth observation and geoinformation, 8*(1), 34–48. https://doi.org/10.1016/j.jag.2005.05.003.

Tu, Y.-K., Kellett, M., Clerehugh, V., & Gilthorpe, M. S. (2005). Problems of correlations between explanatory variables in multiple regression analyses in the dental literature. *British Dental Journal, 199*(7), 457–461. https://doi.org/10.1038/sj.bdj.4812743.

Ullah, S., Tahir, A. A., Akbar, T. A., Hassan, Q. K., Dewan, A., Khan, A. J., & Khan, M. (2019). Remote sensing-based quantification of the relationships between land use land cover changes and surface temperature over the lower Himalayan region. *Sustainability, 11*(19), 5492. https://doi.org/10.3390/su11195492.

Waldmann, P., Mészáros, G., Gredler, B., Fuerst, C., & Sölkner, J. (2013). Evaluation of the lasso and the elastic net in genome-wide association studies. *Frontiers in Genetics, 4*, 1–11. https://doi.org/10.3389/fgene.2013.00270.

Walter, V. (2004). Object-based classification of remote sensing data for change detection. *ISPRS Journal of Photogrammetry and Remote Sensing, 58*(3–4), 225–238. https://doi.org/10.1016/j.isprsjprs.2003.09.007.

Wang, C., Wang, Z.-H., Wang, C., & Myint, S. W. (2019). Environmental cooling provided by urban trees under extreme heat and cold waves in US cities. *Remote Sensing of Environment, 227*, 28–43. https://doi.org/10.1016/j.rse.2019.03.024.

Wu, J. (2004). Effects of changing scale on landscape pattern analysis: Scaling relations. *Landscape Ecology, 19*(2), 125–138. https://doi.org/10.1023/B:LAND.0000021711.40074.ae.

Xiao, R., Weng, Q., Ouyang, Z., Li, W., Schienke, E. W., & Zhang, Z. (2008). Land surface temperature variation and major factors in Beijing, China. *Photogrammetric Engineering & Remote Sensing, 74*(4), 451–461. https://doi.org/10.14358/PERS.74.4.451.

Yang, J., McBride, J., Zhou, J., & Sun, Z. (2005). The urban forest in Beijing and its role in air pollution reduction. *Urban Forestry & Urban Greening, 3*(2), 65–78. https://doi.org/10.1016/j.ufug.2004.09.001.

Yoo, W., Mayberry, R., Bae, S., Singh, K., He, Q. P., & Lillard, J. W., Jr (2014). A study of effects of multicollinearity in the multivariable analysis. *International journal of applied science and technology, 4*(5), 9–19. https://www.ncbi.nlm.nih.gov/pmc/articles/PMC4318006/.

Zhang, X., Zhong, T., Feng, X., & Wang, K. (2009). Estimation of the relationship between vegetation patches and urban land surface temperature with remote sensing. *International Journal of Remote Sensing, 30*(8), 2105–2118. https://doi.org/10.1080/01431160802549252.

Zhang, Y.-J., Yi, W.-C., & Li, B.-W. (2015). The impact of urbanization on carbon emission: Empirical evidence in Beijing. *Energy Procedia, 75*, 2963–2968. https://doi.org/10.1016/j.egypro.2015.07.601.

Zhang, Y., & Sun, L. (2019). Spatial-temporal impacts of urban land use land cover on land surface temperature: Case studies of two Canadian urban areas. *International Journal of Applied Earth Observation and Geoinformation, 75*, 171–181. https://doi.org/10.1016/j.jag.2018.10.005.

Zheng, B., Myint, S. W., & Fan, C. (2014). Spatial configuration of anthropogenic land cover impacts on urban warming. *Landscape and Urban Planning, 130*, 104–111. https://doi.org/10.1016/j.landurbplan.2014.07.001.

Zhou, W., Huang, G., & Cadenasso, M. L. (2011). Does spatial configuration matter? Understanding the effects of land cover pattern on land surface temperature in urban landscapes. *Landscape and Urban Planning, 102*(1), 54–63. https://doi.org/10.1016/j.landurbplan.2011.03.009.

Zhou, W., Wang, J., & Cadenasso, M. L. (2017). Effects of the spatial configuration of trees on urban heat mitigation: A comparative study. *Remote Sensing of Environment, 195*, 1–12. https://doi.org/10.1016/j.rse.2017.03.043.

Zou, H., & Hastie, T. (2005). Regularization and variable selection via the elastic net. *Journal of the Royal Statistical Society: Series B (Statistical Methodology), 67*(2), 301–320. https://doi.org/10.1111/j.1467-9868.2005.00503.x.